IR-induced second-harmonic generation in PbSe microcrystallites

2004 J. Phys.: Condens. Matter 16 3533

(http://iopscience.iop.org/0953-8984/16/21/003)

INSTITUTE OF PHYSICS PUBLISHING JOURNAL OF PHYSICS: CONDENSED MATTER

J. Phys.: Condens. Matter **16** (2004) 3533–3544 PII: S0953-8984(04)76507-8

IR-induced second-harmonic generation in PbSe microcrystallites

I V Kityk[1], M Demianiuk[2], A Majchrowski[2], J Ebothé[3] and P Siemion[4]

[1] Department of ZiM, Technological University of Czestochowa, Armii Krajowej 17/19, PL-42201 Czestochowa, Poland
[2] Institute of Applied Physics, Military University of Technology, 2 Kaliskiego Str., 00-908 Warsaw, Poland
[3] Universite de Reims, UFR Sciences, Laboratoire de Microscopies et d'Etude de Nanostructures, BP.138, 51685 Reims Cedex 02, France
[4] Institute of Chemistry WSP, Częstochowa, Aleja Armii Krajowej 13/15, Poland

E-mail: i.kityk@wsp.czest.pl

Received 18 February 2004
Published 14 May 2004
Online at stacks.iop.org/JPhysCM/16/3533
DOI: 10.1088/0953-8984/16/21/003

Abstract

The IR-induced second-harmonic generation in PbSe microcrystallites with sizes of 10–30 nm is observed for the first time. A phenomenological approach of the IR picosecond nonlinear optical response in PbSe is developed for the middle-IR spectral range (5–15 μm). A model reproducing the basic features of experimental data related to second-order optical nonlinearity caused by photoinduced electron–phonon anharmonic interactions is proposed. The model is based on the band structure calculations and photoinduced kinetics with account taken of electron–phonon anharmonic interactions.

(Some figures in this article are in colour only in the electronic version)

1. Introduction

It is well known that the second-order nonlinear optical effects such as second-harmonic generation (SHG) are prevented by symmetry [1] in centrosymmetric materials. An external electric field is usually applied to induce the non-centrosymmetry (electroinduced second-order effects) [2]. Unfortunately, this method cannot be applied for infrared (IR) (narrow-band) materials that are transparent in the middle-IR spectral region, due to appearance of electroconductivity. Another method for creation of acentric media consists in the optical poling method [3]. In particular, it was shown in the silica glasses that there exists a possibility of creation of non-centrosymmetry due to interaction of the bicolour coherent beams. One of the possible explanations was given with account taken of the photo-galvanic

and photoconductivity effects [4, 5]; however, it is difficult to apply for the narrow band semiconductors and to the non-coherent photoinduced processes.

However, the possibility of operating by the material optical constants in this specific spectral range is very important in order to use them as IR optical fibres for CO and CO_2 lasers [6].

Optical poling [7] in centrosymmetric IR materials like PbSe becomes increasingly attractive, since it offers materials for optically operated waveguides using in recording and transmission of IR information. To date all the investigations, including the femtosecond regime, were performed for the near-IR (<3 μm wavelengths) [8, 9]. Among the IR materials, chalcohalides and chalcogenides [10–12] are very promising. The photoinduced changes in these materials, particularly in glass forms, are well studied for the visible and near-IR spectral range [11]. However, the physical origin of the photoinduced changes and those of their second-order nonlinear optical properties are quite different for the middle-IR spectral range. The main reason consists in the commensurability of the middle-IR frequencies with the phonon ones [11]. Consequently, one can expect a substantial contribution of optically induced electron–phonon interactions (EPIs) to the second-order nonlinear optical susceptibilities [11]. The EPIs are described by the third-order derivatives of the electrostatic potential [13]. In this case, the second-order nonlinear optical effects might be enhanced [14]. However, emerging from general phenomenological consideration [15] one can expect a necessity to introduce the nonlinear optical susceptibilities of higher orders.

In this paper, a new type of IR optical poling consisting in photo-pumping of appropriate phonon and electronic states by means of infrared pulse CO lasers ($\lambda = 5.5$ μm) is proposed. Particular care is taken in the study of pump–probe dynamics. A novel nonlinear optical effect associated with the IR photoinduced anharmonic lattice–electron interactions was observed. As a consequence, there appears optically induced electron–phonon anharmonic non-centrosymmetry in the electronic charge density distribution of particular PbSe structural clusters. In the traditional all-optical technique [12], this method is based on three basic physical principles: a net orientation of particular clusters, a photoexcited resonance-selective excitation and an electric-field-induced SHG. In the case of the IR optical poling, the photoinduced non-centrosymmetry of the photoexcited phonons begins to play a key role. Hence, it is necessary to consider a process of interaction between at least two photons and three photoinduced phonons (created by the electrostriction) or a fifth-order process.

In section 2 we present the principal theoretical considerations for understanding the nature of the observed phenomenon. Section 3 is devoted to the experimental method and obtained results; section 4 is devoted to discussion of the obtained results and to the clarification of physical insight into the phenomenon observed.

2. Theoretical consideration

2.1. General phenomenology

Because the non-centrosymmetric photoinduced EPI anharmonicity requires participation of at least three phonons, the SHG effect should be described by an equation

$$P_i = \chi_{ijklmn} E_j^{(\omega)} E_k^{(\omega)} E_l^{(\Omega_1)} E_m^{(\Omega_2)} E_n^{(\Omega_3)} \tag{1}$$

where χ_{ijklm} is the fifth-order NLO susceptibility; $E_l^{(\Omega_1)}$, $E_m^{(\Omega_2)}$ and $E_n^{(\Omega_3)}$ are the effective electric fields of the photoinduced phonons, that appeared due to the photo-stimulated electrostriction; $E_{k,j}^{(\omega)}$ are electromagnetic IR beams with polarization k, j, respectively. Microscopic calculations using the Green function method [16, 17] for numerical evaluations of the IR-induced charge density non-centrosymmetry caused by the anharmonic EPI are done.

The performed calculations have shown that the Pb–Se chemical bonds play the predominant role in the corresponding IR-induced optical susceptibilities. This aspect is developed more deeply within the framework of a dielectric chemical bond method of SHG coefficient evaluation introduced in [18], where it was clearly shown that the individual role of the intra-crystalline chemical bonds should play a crucial role in the observed second-order optical properties. In our case such a role is played by the Pb–Se chemical bonds.

The appearance of a term with frequency 2ω caused by photoinduced non-centrosymmetry is similar to the process of interference between the two coherent waves with the fundamental and doubled frequencies [8]. The temporally averaged output of nonlinear polarization for the doubled frequency may be expressed in the form

$$P^{(2\omega)}(r) \cong \varepsilon_0 |E_{\mathrm{pr}}^{(\omega)}(r, t-\tau)|^2 \{\langle E_{\mathrm{pump}}^{\omega}(r,t)[E^{\Omega_1\pm\Omega_2\pm\Omega_3}(r,t)]^2\rangle + \langle E_{\mathrm{pr}}^{\omega}(r,t)[E^{\Omega_1\pm\Omega_2\pm\Omega_3}(r,t)]^2\rangle + \langle E_{\mathrm{pr}}^{2\omega}(r,t-\tau)[E^{\Omega_1\pm\Omega_2\pm\Omega_3}(r,t)]^2\rangle\} \tag{2}$$

where the brackets mean temporal averaging.

The first term corresponds to interaction between the pumping CO laser beam and the modulated photoexcited non-centrosymmetry anharmonic phonon modes possessing the frequencies, $\Omega_1 \pm \Omega_2 \pm \Omega_3$ (where indices 1, 2 and 3 correspond to the effective frequencies of the phonons participating in the anharmonic interaction process). This term is responsible for appearance of the photoinduced non-centrosymmetry at a given **point** of the media (**r**). The effective amplitudes of the photoinduced phonon modes ($E^{(\Omega_1\pm\Omega_2\pm\Omega_3)}(r,t)$) are proportional to the pumping photoinduced IR power due to the usual electrostriction effect. From the general symmetry considerations of a given cluster, one can conclude that maximal output SHG will be observed for parallel polarization of the pumping and probing beams. This reflects the fact that the direction of the anharmonic charge density shift should be always parallel to the pumping CO laser polarization. The effect of second-order (non-centrosymmetry) appearance may be observed because there exists a range of phonon frequencies satisfying conditions $\omega - \omega_{\mathrm{el}} \pm \Omega_1 \pm \Omega_2 \pm \Omega_3 = 0$, where ω and ω_{el} are frequencies of the pumping and probing electromagnetic IR waves, respectively. This condition is necessary for the occurrence of the non-centrosymmetric tensor components during the picosecond photoexcitation.

Taking into account the nonlinear interactions between a probe wave with wavevector ($k_{\mathrm{pr}}^{(\omega)}$) *and* the double-frequency one ($k^{(2\omega)}$) and the pump wave with frequency $k_{\mathrm{pump}}^{(\omega_p)}$ as well as the photoinduced anharmonic frequencies with the wavevectors ($K^{(\Omega_1\pm\Omega_2\pm\Omega_3)}$), a wide spectrum of angles satisfying the phase matching conditions occurs as follows:

$$P^{(2\omega)}(r,t) \cong \varepsilon_0 \chi^{(5)}(2\omega;\omega,\omega,\Omega_1,\Omega_2,\Omega_3)|E_{\mathrm{pr}}^{(\omega)}(r,t)|^2 \exp[-\mathrm{i}\Delta k r], \tag{3}$$

where

$$\Delta k = k^{(2\omega)} \pm k_{\mathrm{pr}}^{(\omega)} \pm (k_{\mathrm{pump}}^{(\omega p)} \pm K^{(\Omega_1\pm\Omega_2\pm\Omega_3)}). \tag{3a}$$

The range of angles satisfying the phase matching conditions (3*a*) will be relatively large because there exist large groups of phonons satisfying the phase matching conditions within the spectral range 5–8 μm. The performed calculations predict an increase of the photoinduced SHG with an increasing IR-induced intensity and with a decreasing temperature.

2.2. Band structure and molecular dynamics simulations

For simulations of the picosecond photoinduced charge density non-centrosymmetry we have used the method of norm-conserving pseudopotential [19] together with the appropriate molecular dynamics simulations similarly to those presented in [20].

We first estimated the band energy structure of the PbSe crystallites for the given sizes of the crystallites. Starting pseudo-wavefunctions were built using a procedure proposed in [19, 20] for a non-local self-consistent norm-conserving pseudo-potential. Actual 6s, p Pb and 4s, p Se occupied and diffused 7s, p Pb together with the 5s Se and 4d Pb orbitals were taken into account.

The total energy was expressed within a local density functional approximation with respect to the charge density $\rho(\mathbf{r})$:

$$U[\rho(r)] = T[\rho(\mathbf{r})] + V_{\mathrm{n-e}}[\rho(\mathbf{r})] + V_{\mathrm{e-e}}[\rho(\mathbf{r})] + V_{\mathrm{e-c}}[\rho(\mathbf{r})] \tag{4}$$

where

$$\rho(\mathbf{r}) = \sum_{\beta,l} |\Psi(l, \mathbf{r}, \beta)|^2. \tag{5}$$

Here the kinetic charge density functional $T[\rho(r)]$ is calculated within a Thomas–Fermi free electron approximation; $V_{\mathrm{n-e}}[\rho(\mathbf{r})]$ reflects electron–nuclear Coulomb-like interaction which was chosen in the form described in [12]. In equation (1) we also included screened potentials $V_{\mathrm{e-e}}[\rho(\mathbf{r})]$ and $V_{\mathrm{e-c}}[\rho(\mathbf{r})]$, corresponding to electron–electron and exchange–correlation interaction, respectively. A nonlinear extrapolation procedure was carried out in order to calculate the fitting coefficients of the corresponding pseudo-wavefunctions, as well as the derivative pseudopotentials, in a form convenient for analytical evaluations of secular equation matrix elements, particularly

$$\Psi(l, r, \beta) = \sum_{n} a_n^{\beta} r^n \exp[-\alpha_n^{(l,\beta)} r^n] \tag{6}$$

where β denotes atom kind, l is the corresponding angular momentum and n determines the level of precision of the nonlinear fitting procedure and can vary from 1 to 5. The coefficients a^{β} and $\alpha_n^{(l,\beta)}$ are fitting coefficients calculated during the nonlinear fitting procedure. The precision of the fit was, in the best case, 0.03 Hartree.

The pseudopotential was chosen in the following form:

$$V_{\mathrm{ps}}^{(\beta,l)} = \sum_{i=1}^{3} [A_i^{\beta} + r^2 A_{i+3}^{\beta} \exp(-\alpha_l^{(l,\beta)} r^2)] \tag{7}$$

where A_i, A_{i+3}, $\alpha_l^{(l,\beta)}$ are fitting coefficients.

This technique for calculation of matrix elements is described in detail in [9]. We solved the following secular equation corresponding to a pseudopotential given by (7):

$$\left\| [h^2(\mathbf{k} + \mathbf{G}_n)^2/2m - E(\mathbf{k})]\delta_{n,n'} + \sum_{\alpha} V_{\alpha}(\mathbf{G}'_n - \mathbf{G}_n) S_{\alpha}(\mathbf{G}'_n - \mathbf{G}_n) \right\| = 0 \tag{8}$$

where $E(\mathbf{k})$ is the eigenenergy for a $\mathbf{k}$-point in the Brillouin zone and $\mathbf{G}'_n$, $\mathbf{G}_n$ are wavevectors of interacting base plane waves. A structural form-factor takes into account the sizes of the crystallites:

$$S_{\beta}(\mathbf{G}'_n - \mathbf{G}) = g^{(\beta)}/\Omega N_a \sum \exp(-\mathrm{i}(\mathbf{G}'_n - \mathbf{G}_n)\tau_{\beta}). \tag{9}$$

Here $g^{(\beta)}$ is a weighting factor associated with the sizes of the crystallites. A similar superposition of different structural fragments disturbing the perfect crystals has just been successfully used for binary solid alloys, glasses and organic materials [16, 21, 22]. We choose a plane wave basis set consisting of 158–260 plane waves to achieve eigenenergy convergence of 0.023 eV.

The solution of the secular equation set was obtained using a modified Jacobi method QL. Additional (180–230) plane waves from an extended base were incorporated into our

calculations within the framework of a Lowdin perturbation approach. A Fourier transform of the pseudopotential has taken the form

$$V_\alpha(\mathbf{G}'_n - \mathbf{G}_n) = 1/W \int V_\alpha(\mathbf{r}) \exp[-\mathrm{i}(\mathbf{G}'_n - \mathbf{G}_n)r]. \tag{10}$$

Electron screening effects were incorporated using a parametrized Perdew–Zunger expression in the following form:

$$\mu_{xc} = -0.6193/r_s - 0.143\,92/(1 + 1.0529r_s^{1/2} + 0.3334r_s) \times \{1 + [(0.526r_s^{1/2} + 0.3334r_s)/(3(1 + 1.0529r_s^{1/2} + 0.3334r_s))]\} \quad \text{for } r_s > 1 \tag{11}$$

$$\mu_{xc} = -0.6193/r_{ss} + 0.031\ln(r_s) - 0.0583 \qquad \text{for } r_s < 1 \tag{12}$$

where $r_s = [3/(4\pi\rho)]^{1/3}$ with ρ being electron density. The special Chadhi–Cohen point method was applied for calculation of the electron charge density distribution. A diagonalization procedure was carried out at special weighting points for each structural cluster.

Acceleration of the iteration convergence was achieved by transferring 75% of the $(m-1)$th iteration result to the mth iteration. The following condition was taken as the criterion for self-consistency:

$$|(\rho_m - \rho_{m-1})/\rho_m| < \varepsilon. \tag{13}$$

We assumed a level of calculation error (ε) better than 0.12%. The level of agreement with previously undertaken calculations of the electron density of states within a framework of LMTO or pseudopotential methods was equal to about 0.3 eV. However, the main drawback of all one-electron calculations consists in an underestimation of the bandgap values. For this reason self-energy correction renormalization was carried out during the band structure calculations. As a result, the total energy deviation in relation to the energy cut-off and the Perdew–Alder screening parameter was stabilized to 0.22 eV.

To carry out the geometry optimization, we used the molecular dynamics technique described in [20]. Due to the high level of IR pump density, when estimating the evolution of the corresponding levels, we focus first on the evolution of the ground molecular N_1 level. For convenience, the corresponding set of kinetic equations is presented in the form

$$\begin{aligned} \mathrm{d}N_1/\mathrm{d}t &= -B_{12}\rho N_1 - B_{12}B_{23}\rho^2 N_1 + A_{31}N_3 + A_{41}N_4 \\ \mathrm{d}N_3/\mathrm{d}t &= B_{13}\rho N_3 + B_{12}B_{23}\rho^2 N_1 + A_{34}N_3 - A_{31}N_3 \\ \mathrm{d}N_4/\mathrm{d}t &= B_{14}\rho N_1 - B_{12}A_{34}B_{23}\rho^2 N_1 + A_{31}N_3 - A_{41}N_4 \end{aligned} \tag{14}$$

A and B are used to indicate the spontaneous and optically induced Einstein coefficients between the respective levels.

For convenience, the equation for N_1 can be presented in the form

$$\mathrm{d}N_1/\mathrm{d}t = -\gamma I^2 N_1 + aN_4. \tag{15}$$

In this case we include linear absorption as a background independent of the external light, and assume that trapping from the EPI sublevels is very fast and complete. At the beginning we did not, therefore, consider the metastable states due to EPI. The solution for this equation takes the form

$$N_1 = aN/(\beta + a) + \beta N/(\beta + a)\exp(-(\beta + a)t) \tag{16}$$

where $N_1 + N_4 = N$ and $\beta = \gamma I^2$. At the first stage we considered pure electronic and EP states as simply superimposed, and only afterwards took into account the contribution of the secondary piezoelectric and electrostricted effects.

We would emphasize that in the following analysis we do not take into consideration the complicated structure of the effective bands 3 and 4 (in particular, the contribution of levels with a longer lifetime). The expression for the N_1 level, which is the basis for this process, can be written as

$$N_1 = -N_1(0)\exp(-B_{12}\rho)t \tag{17}$$

and the level of the particular population is expressed in the form

$$\begin{aligned} N_1 = {} & (A_{31}N_3 - A_{41}N_4)/(B_{12}B_{23}\rho^2 N_1 + A_{31}N_3 - A_{41}N_4) \\ & + B_{12}B_{23}\rho^2 N_1/(B_{12}B_{23}\rho^2 N_1 + A_{34}N_3 - A_{41}N_4) \\ & \times \exp[-(B_{12}B_{23}\rho^2 N_1 + A_{31}N_3 - A_{41}N_4)t]. \end{aligned} \tag{18}$$

The qualitative estimations based on a simplified molecular dynamics approach suggest the possibility that several maxima may occur in the picosecond time-delay range of the SHG. So we have also taken into account the photoexcited two-photon states. However, our estimations have shown that their contribution is below 8%.

In order to investigate the possible role played by EPI contributions, we carried out calculations for a base set renormalized by electron subsystems. Second derivatives of the electrostatic cluster potential with respect to given normal coordinates were calculated numerically with precision up to 0.0028 Hartree for the main chemical bonds. These calculations were used to determine the force constants.

The electron–phonon interaction potential was calculated in a nonlinear approximation:

$$V_{\mathrm{e-ph}}(\mathbf{r}_i) = e^2 \sum_{ms} M_{ms}^{-\frac{1}{2}} \left[Z_{ms}(\mathbf{r}_s - \mathbf{u}_{ms})|\mathbf{r}_s - \mathbf{u}_{ms}|^{-\frac{1}{3}} - \sum_{m's'} Z_{m's'}(\mathbf{r}_{s'} - \mathbf{u}_{m's'})|\mathbf{r}_{s'} - \mathbf{u}_{m's'}|^{-3} \right] \tag{19}$$

where M_{ms} and eZ_{ms} are the effective ionic mass and charge of Pb and Se. The corresponding ions are numbered by m and s, respectively. The $\mathbf{u}_{ms,m's'}$ vector is the relative displacement of two ions from their equilibrium positions $\mathbf{r}_s$ and $\mathbf{r}_{s'}$. The probability of a one-phonon transition is given by

$$W(\Omega_k) = 4\left(\frac{h}{2\pi}\right)^{-2} c^{-3} H^{-1} g^{-1}(\mathbf{r}_i)(E - \Omega_k)^2 B(\Omega_k) \tag{20}$$

where η and ξ are the lower and upper electron MO energy levels, respectively; H is the sum of the η and ξ level widths, E is the energy of the UV photoinducing beam, Ω_k denotes the kth phonon energy and $g(r_i)$ is the degeneration factor of the corresponding electron energy levels.

The parameter $B(\Omega_k)$ is given by

$$\begin{aligned} B(\Omega_k) = \sum_{\eta} g(\eta) \sum_{\xi} g(\xi) \Bigg| \Bigg\{ & \sum_{\varphi} \langle \eta, \eta_\Omega | V_{\mathrm{e-ph}}(\mathbf{r}_i) | \varphi, \eta_{\Omega+1} \rangle \langle \varphi | \mathbf{d} | \xi \rangle (E_\xi - E_\eta + \Omega_k)^{-1} \\ & + \sum_{\varphi} \langle \eta | \mathbf{d} | \varphi \rangle \langle \varphi, \eta_\Omega | V_{\mathrm{e-ph}}(\mathbf{r}_i) | \xi, \eta_{\Omega-1} \rangle (E_\xi - E_\eta - \Omega_k)^{-1} \Bigg\} \Bigg|^2 \theta \end{aligned} \tag{21}$$

where φ denotes a virtual intermediate excited quasi-phonon state and $\mathbf{d}$ is the electric dipole moment for a given optical transition; η_Ω and η, φ, ξ correspond to electronic and phonon states respectively. The summation was carried out over all degenerate initial and final states. θ denotes the average with respect to the degree of occupation of the quasi-phonon states with frequency Ω_k.

The occupation dynamics caused by IR-induced changes was calculated using the following electron–quasi-phonon population differential equations:

$$\mathrm{d}n_0/\mathrm{d}t = -\sum_{\alpha} A_{0\alpha} \int [B_{0\alpha}(t-\tau)\ln_{\alpha}] + \sum_{\alpha}(A_{0\alpha}n_{\alpha}) \tag{22}$$

$$\mathrm{d}n_{\alpha}/\mathrm{d}t = -\sum_{\beta} A_{\beta\alpha} \int [B_{\beta\alpha}(t-\tau)\ln_{\beta}] + \sum_{\beta}(A_{\beta\alpha}n_{\alpha}) \tag{22a}$$

where I is the photoinducing power density; n_{α} is the population of the αth state; τ is the time delay between the pump and probe beams. $B_{0\alpha}$ and $A_{0\alpha}$ are, respectively, the induced and spontaneous Einstein coefficients between the ground (0) and excited (α) states:

$$\begin{aligned} A_{0\alpha} &= 8\pi\omega^3|\mathbf{d}_{0\alpha}|^2 n_{\mathrm{e}0}n_{\mathrm{ph}0}(1-n_{\mathrm{e}\alpha})(1-n_{\mathrm{ph}\alpha})/3hc^3 \\ B_{0\alpha} &= c^3A_{0\alpha}/\pi h\omega^3. \end{aligned} \tag{23}$$

Here $n_{\mathrm{e}0}$ and $n_{\mathrm{ph}0}$ correspond to the Fermi–Dirac and Bose–Einstein carrier distributions of the ground state for electronic and phonon states, respectively. This expression takes into consideration the influence of pump power density through the photoinduced phonons. We considered 56 coupled IR phonon oscillators resolving the same number of equations.

In order to understand the temperature dependences, we considered the contributions of harmonic, as well as anharmonic, EPI:

$$B^{-}(\Omega_k) = C_{\eta}\xi^{\gamma}(r_{\lambda}^{\delta})C_{\eta}\xi^{\gamma'}(r_{\lambda'}^{\delta'})\,\mathrm{Im}\,G_{\Delta\Delta'}^{\gamma\gamma'}(r_{\lambda}^{\delta},\Omega_k^2) \tag{24}$$

where $G_{\Delta\Delta'}^{\gamma\gamma'}(r_{\lambda}^{\Delta})$ is the Green function (γ and γ' are numbers of the coordination sphere) defined as

$$G_{\Delta\Delta'}^{\gamma\gamma'}(r_{\lambda}^{\Delta}) = \sum_{\varphi}\{\langle|V_{\mathrm{e-ph}}(r_i)|\varphi\rangle\langle\varphi|\mathbf{d}|\xi\rangle + \langle\eta|\mathbf{d}|\varphi\rangle\langle\varphi|V_{\mathrm{e-ph}}(r_i)|\xi\rangle\}(E_{\xi}-E_{\eta})^{-1}. \tag{25}$$

The resulting expression is given below:

$$G_{\Delta\Delta'}^{\gamma\gamma'}(r_{\lambda}^{\delta},\Omega_k^2) = \sum_{\Omega} K_{\Delta'}^{\gamma'}(r_{\lambda}^{\Delta})K_{\Delta}^{\gamma}(r_{\lambda}^{\Delta})(\Omega_k^2-\Omega^2-\mathrm{i}\delta)^{-1} \tag{25a}$$

where the coordinates $K_{\Delta}^{\gamma}(r_{\lambda}^{\Delta})$ are obtained for a given averaged level of phonons. Numerical calculations were made with an accuracy up to 0.019 Hartree.

To include the IR-induced lattice deformations within the Green function, we took into account IR-induced deformation localization through the piezoelectric and electrostricted relations, allowing us to apply the Dyson relations as in [20].

The potential operator U was determined by the IR-induced potential deformation and corresponding disturbance caused by the charge defect. Thus

$$G_{\Delta\Delta'}^{\gamma\gamma'}(1) = G_{\Delta\Delta'}^{\gamma\gamma'}(0) + G_{\Delta\Delta'}^{\gamma\gamma'}(0)UG_{\Delta\Delta'}^{\gamma\gamma'}(1) \tag{26}$$

where $G_{\Delta\Delta'}^{\gamma\gamma'}(0)$ is the Green function for harmonic subsystems, and $G_{\Delta\Delta'}^{\gamma\gamma'}(1)$ is the Green function for subsystems disturbed by the IR-induced anharmonic electron-vibration potential U.

The performed calculations allowed us to determine the parameters of the dipole moments and inter-band levels with temperature, which allowed us to apply the methods of the second-order hyperpolarizability calculations similarly as in [17].

As a consequence we have obtained in figure 1 theoretically calculated contours of the expected second-order susceptibilities for $\lambda = 10.6$ μm SHG versus temperature and IR pump power density. One can see that the SHG should possess a non-monotonic dependence on the temperature and IR-induced power. Such dependences are a consequence of the

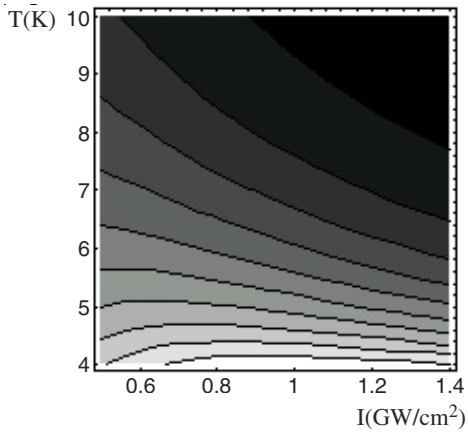

Figure 1. Contour plot of theoretically calculated second-order optical susceptibilities d_{xxx} versus photoinducing CO laser power (**I**) and temperature (**T**). Every shadowing step corresponds to 0.2 μm V^{-1}.

crucial role played by the IR-induced anharmonic phonon modes, particularly due to the Pb–Se phonon modes, which show substantial dependence on the intensity of the external polarized light. At the same time these modes are nonlinearly dependent on temperature (due to complicated temperature dependences of the anharmonic phonon modes), which gives the observed sequence of temperature–pump power dependences.

3. Experimental results

3.1. Sample preparation

For an experimental verification of the proposed theoretical approach we have synthesized PbSe crystals. The Bridgman technique was used to grow PbSe crystals from graphite crucibles under argon ambient atmosphere (5 MPa). The details of the technology were described by Demianiuk [23]. As-grown crystals had diameter and length of 10 and 60 mm, respectively. The microscopic and x-ray diffractometer investigations revealed that the obtained PbSe crystals were built of 10–30 nm sized microcrystallites creating a morphological crystallite background [23].

Moreover, the independently performed AFM control of the morphology has shown that during the IR pumping no evidence of structural change was found.

3.2. Experimental set-up

The experimental SHG was determined by the Maker fringe method [19] for the 280 μm thick samples. The principal experimental set-up is presented in figure 2. The equipment allowed the performance of the IR-poled optical SHG measurements. The pulsed CO laser ($\lambda = 5.5$ μm; $P =$ 12–28 MW; $\tau =$ 0.44–80 ps, frequency repetition 8–15 Hz) served as an IR pumping light. We used a Q-switched CO_2 laser beam ($\lambda = 10.6$ μm; $P = 25$ MW; $\tau =$ 2–10 ps) for the SHG as the probing beam. This laser was synchronized in time with the CO laser beam ($\lambda = 5.5$ μm). The pumping CO laser energy was chosen to avoid the specimen overheating. An IR liquid-helium-cooled HgCdTe fast response photodetector, which was connected to a boxcar (gain time up to 420 ps), was used for the detection of the output SHG signal. The laser beams were scanned through the surface to average the specimen's surface non-homogeneity

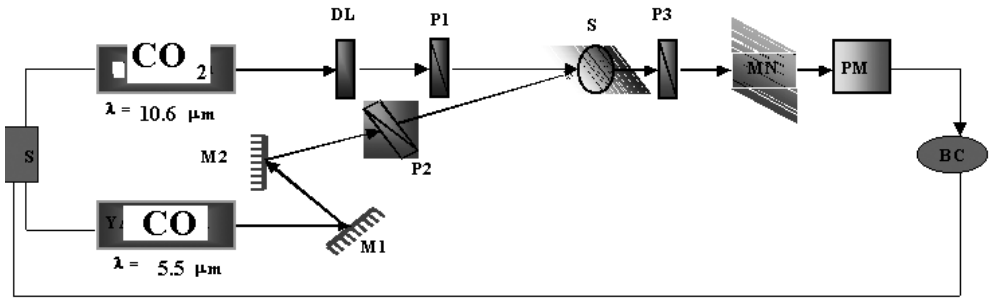

Figure 2. Principal experimental set-up for the IR-induced SHG measurements: **DL**, delaying line; **P1**, **P2** and **P3** are polarizers; **S**, investigated samples; **MN**, monochromator; **PM**, photomultiplier; **BC**, boxcar; **S**, synchronizer.

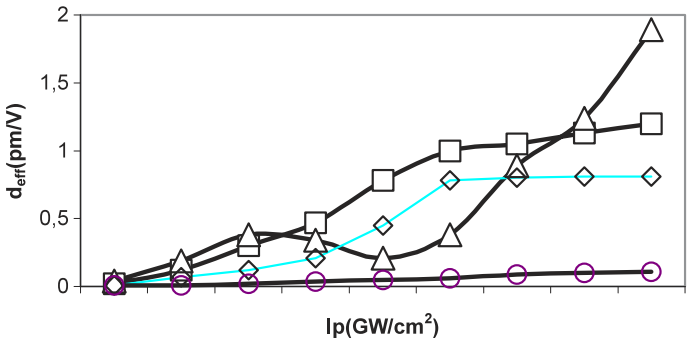

Figure 3. The experimentally evaluated second-order optical susceptibility d_{xxx} dependences on the pumping CO laser power I at different temperatures: △—$T = 4.2$ K; □—$T = 10$ K; ◇—25 K; ○—the same for the off-diagonal d_{xyz} tensor component at $T = 4.2$ K.

with varying incident angle within the range $-20°$ to $20°$. The Maker fringe pattern possessed good symmetry and the SHG output signal achieved its maximum at angles lying within the range 35°–55°. The output SHG was varied within the range 10^{-4}–10^{-6} compared to the incident beam (signal). The calculations of the SHG tensor susceptibilities were done taking into account Fresnel losses, the Gaussian-like profile of the beam and optical attenuation as well as the appearance of the photoinduced birefringence (10^{-1}–10^{-2}). The performed calculations showed that the maximal output SHG exists for the parallel polarization of inducing and probing laser beams. The angle between these beams should not exceed 5.6°. The fluorescent signal appeared for the spectral wavelengths below 3.2 μm and was spectrally slightly separated by a grating IR monochromator (spectral resolution 9 nm mm^{-1}). The time duration of the SHG signal was about 4 ps.

In figure 3, the measured dependences of the second-order susceptibility ($d^{(2\omega)}$) ($\lambda = 10.6$ μm) (evaluated from the SHG intensities) on CO laser pump power ($\lambda = 5.5$ μm) are presented. An increase of the photoinduced SHG with the increase of the pumping CO laser powers within 0–1.5 GW cm^{-2} was revealed. Even for the temperature of 4.2 K, a good agreement with the theoretically calculated dependences (compare with the figure 1) was achieved.

With decreasing temperature the photoinduced SHG increases, achieving relatively large values (up to 5.0 pm V^{-1}; average value 2 pm V^{-1}). The diagonal tensor component values

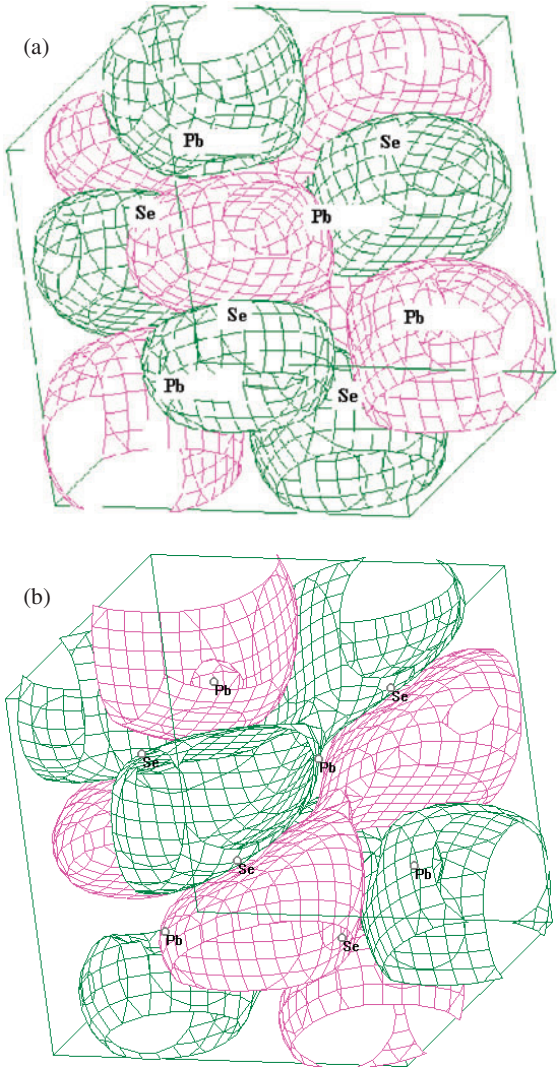

Figure 4. Photoinduced changes of the electrostatic charge density distribution: (a) without account taken of the anharmonic electron–phonon interactions; (b) with account taken of the anharmonic electron–phonon interactions. Different colours correspond to different signs of the electrostatic field changes.

are larger than all the off-diagonal tensor components by about one order. For the pumping powers higher than 1.6 GW cm^{-2} photochemical destruction has appeared. A good agreement between theoretical curves and experimental results is observed.

The fluorescent spectra showed a signal in the spectral range of 1.2–3 μm. In fact, it is outside the range of the fundamental and doubled frequency spectral region. Maximal SHG signal was observed for the pump–probe delaying times of about 28 ps.

4. Discussion

To understand the physical insight of the phenomenon observed we have used an approach described in section 2, calculating the IR-induced changes within the PbSe crystallites at a

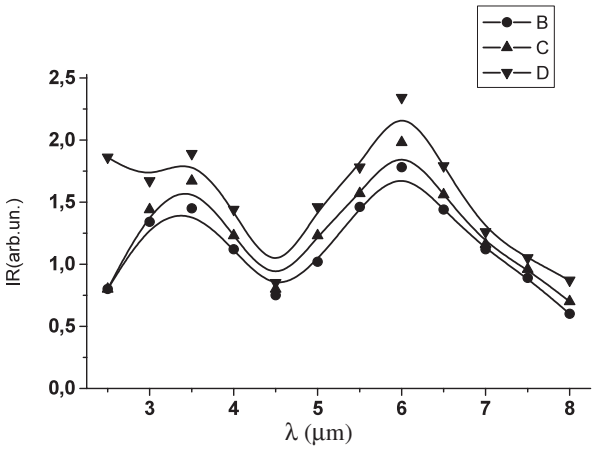

Figure 5. Photoinduced spectral dependence of the photoinduced IR mode density changes: **B**—0.5 GW cm^{-2}; **C**—1.0 GW cm^{-2}; **D**—1.5 GW cm^{-2} at 4.2 K.

pump power of about 1 GW cm^{-2} and for a delaying time of about 28 ps. In figures 4(a) and (b) are presented the mentioned photoinduced charge density re-distribution predicted with and without account taken of the EPI. The different colours correspond to the different electrostatic potential changes. The appearance of the acentric charge density distribution is obvious for the anharmonic EPI.

One can clearly see an occurrence of additional charge density non-centrosymmetry during consideration of the IR-induced EPI. This fact is a crucial argument confirming the crucial role of the anharmonic EPI. It is important to say that the increasing pump power leads to additional charge density non-centrosymmetry and the maximal non-centrosymmetry is observed at times of about 30 ps in agreement with the pump–probe delaying experiments.

To confirm theoretical predictions on the dominant role of the EPI, the IR spectra within the 4–7 μm range were measured under the influence of CO laser pumping beams at $T = 4.2$ K (see figure 5). One can see that the increasing CO laser photoinducing beams favours the appearance of additional IR modes within the spectral ranges 3–7 μm. Such an increase correlates well with the observed second-order optical effects. This is a direct confirmation of the substantial contribution of the EPI to the output nonlinear optical susceptibilities performed theoretically (compare with figure 1). The existence of steplike dependences reflects the existence of crystallite morphology.

Achieving sufficiently good agreement between the simulated and experimentally measured data indicates mechanisms which may be more general than for the considered PbSe microcrystallites. One can expect that the phenomenon observed should be extended to a larger number of the narrow-band crystallites and may open a possibility of their use in IR optoelectronics.

5. Conclusions

In summary, the macroscopic IR-induced nonlinear optical effects in polycrystalline PbSe were found. Band structure calculations and photoinduced electron–phonon anharmonicity indicate a crucial role of the IR-induced anharmonic electron–phonon interactions in the observed effect. The value of the observed IR-induced second-order susceptibility is relatively large and achieves a value of up to 5 pm V^{-1} at $\lambda = 10.6$ μm. Independent measurements of

the photoinduced IR spectra directly indicate a good correlation between the number of the photoexcited IR modes and the observed SHG, confirming thus the substantial role of the anharmonic electron–phonon interactions. The time evolution of these effects is consistent with a simple model of electron–phonon anharmonic interactions. The IR poling surely opens a new perspective in the tailoring of phase-matching glasses for frequency conversion.

Acknowledgments

The work was partially supported by grants GU3 WMP 39-00 (IVK) and 4T08A 007 22 (AM) of the Polish Committee for Scientific Research (KBN). We are grateful to Professor J Koziol (WSP Czestochowa) for the opportunity to perform the optical measurements.

References

[1] Bloembergen N 1965 *Nonlinear Optics* (New York: Benjamin)
Boyd R W 1992 *Nonlinear Optics* (Boston, MA: Academic)
[2] Chemla D S and Zyss J 1986 *Nonlinear Optical Properties of Organic Molecules and Crystals* vol 1 and 2 (New York: Academic)
[3] Antonyuk B P, Antonyuk V B, Musichenko S F and Podobedov V P 1996 *Phys. Lett.* A **213** 297
[4] Kazansky P G and Pruneri V 1997 *Phys. Rev. Lett.* **78** 2956
[5] Balakirev M K, Smirnov V A, Vostrikova L I, Kityk I V, Kasperczyk J and Gruhn W 2003 *J. Mod. Opt.* **50** 1237
[6] Homoelle D, Wielandy S, Gaeta A L, Borelli N F and Smith C 1999 *Opt. Lett.* **24** 1311
Grubsky V and Feinberg J 2000 *Opt. Lett.* **25** 203
Stegall D B and Erdogan T 2000 *J. Opt. Soc. Am.* A **17** 304
[7] Dodge J S, Schumacher A B, Bigot J-Y, Chemla D S, Inglr N and Beasley M R 1999 *Phys. Rev. Lett.* **83** 4650
Gautier C A, Lefumeux C, Albert O and Etchepare J 2000 *Opt. Commun.* **178** 217
[8] Antonyuk B P 2000 *Opt. Commun.* **181** 191
[9] Primozich N, Shahbazyan T V, Perakis I E and Chemla D S 2000 *Phys. Rev.* B **61** 2041
[10] Zhao X, Xu L, Yin H and Sakka S 1994 *J. Non-Cryst. Solids* **167** 70
Kityk I V, Kasperczyk J and Plucinski K 1999 *J. Opt. Soc. Am.* B **16** 1719
[11] Kityk I V and Sahraoui B 1999 *Phys. Rev.* B **60** 942
[12] Hisakuni H and Tanaka K 1994 *Appl. Phys. Lett.* **65** 2925
Schaafsma D T, Shaw L B, Cole B, Sanghera J S and Aggarwal I D 1998 *IEEE Photon. Technol. Lett.* **10** 1548
Frumar M, Polak Z and Cernosek Z 1999 *J. Non-Cryst. Solids* **257** 105
Wasylak J, Kucharski J, Kityk I V and Sahraoui B 1999 *J. Appl. Phys.* **85** 425
Quiquempois Y, Villeneuve A, Dam D, Turcotte K, Muller J, Stegeman G and Lacroix S 2000 *Electron. Lett.* **36** 733
Lopez-Lago E, Couderc V, Griscom L, Smektala F and Barthelemy A 2000 *CLEO/Europe-IQEC 2000 (Nice, France, Sept. 2000)* Paper CThC6
[13] Dalal N, Klymachyov A and Bussmann-Holder A 1998 *Phys. Rev. Lett.* **81** 5924
[14] Napieralski J 1999 *Ferroelectrics* **220** 17
[15] Kityk I V 1992 *Sov. Techn. Lett.* **16** 235
[16] Sahraoui B, Kityk I V, Nguyen Phu X, Hudhomme P and Gorgues A 1999 *Phys. Rev.* B **59** 9229
[17] Kityk I V 1991 *Phys. Solid State* **26** 1026
[18] Xue D, Betzler K and Hasse H 2000 *Phys. Rev.* B **62** 13546
[19] Bachelet G B, Hamann D R and Schluter M 1982 *Phys. Rev.* B **26** 4199
Kityk I V, Kasperczyk J and Andrievskii B V 1996 *Phys. Lett.* A **216** 161
[20] Kityk I V 2003 *Semicond. Sci. Technol.* **18** 1001
[21] Kityk I V 2003 *Mater. Lett.* **57** 1798
[22] Kityk I V 2003 *Comput. Mater. Sci.* **27** 342
[23] Demianiuk M 1990 *Mater. Res. Bull.* **25** 337